



Interfacial engineering and hydrophilic/aerophobic tuning of Sn₄P₃/Co₂P heterojunction nanoarrays for high-efficiency fully reversible water electrolysis

Xinyu Qin ^{a,1}, Bingyi Yan ^{a,1}, Dongwon Kim ^{a,1}, Zhishun Teng ^b, Tianyu Chen ^a, Juhyung Choi ^a, Lin Xu ^{b,*}, Yuanzhe Piao ^{a,c,**}

^a Department of Transdisciplinary Studies, Graduate School of Convergence Science and Technology, Seoul National University, 145, Gwanggyo-ro, Yeongtong-gu, Suwon-si, Gyeonggi-do, Republic of Korea

^b School of Chemistry and Materials Science, Jiangsu Key Laboratory of New Power Batteries, Jiangsu Collaborative Innovation Centre of Biomedical Functional Materials, Nanjing Normal University, Nanjing 210023, PR China

^c Advanced Institutes of Convergence Technology, Seoul National University, 145, Gwanggyo-ro, Yeongtong-gu, Suwon-si, Gyeonggi-do, Republic of Korea



ARTICLE INFO

Keywords:

Transition metal phosphide
Interface engineering
Hydrophilic/aerophobic
Overall water splitting

ABSTRACT

The simultaneous integration of electronic regulation and architectural engineering in one electrocatalyst represents a powerful leverage to concurrently boost the electrocatalytic performance towards overall water splitting. We herein rationally fabricate Sn₄P₃/Co₂P “stalk”-“cap”-typed nanoarrays (Sn₄P₃/Co₂P SCNA) with abundant heterointerfaces and elaborately implanted “caps”. The nanoarrayed structure can substantially enlarge the exposure of active sites and promote the mass/electron transport, thus accelerating the reaction kinetics. Moreover, the purposely grafted “caps” are beneficial to increase the hydrophilicity/aerobicity, which facilitate the water affinity and release of generated gas bubbles. Accordingly, the obtained Sn₄P₃/Co₂P SCNA deliver exceptional electrocatalytic performances towards the HER and OER, as reflected by the overpotentials of 45.4 and 280.4 mV at 10 mA cm⁻², respectively. More impressively, the two-electrode electrolyzer assembled by freestanding Sn₄P₃/Co₂P SCNA requires a cell voltage of 1.56 V at 10 mA cm⁻² and exhibits superior stability and full reversibility, holding great potential in practical water electrolysis.

1. Introduction

The ever-growing global demand for clean and sustainable energy sources has stimulated the enormous endeavors to develop renewable and zero-emission energy carriers as traditional fossil fuel alternatives. Hydrogen has been unquestionably acknowledged as the most ideal energy carrier on account of its superb energy density, carbon-free footprint and perfect recyclability [1]. As compared with the conventional steam reforming process for H₂ production, the water electrolysis technology has attracted ever-increasing attention due to its prominent superiorities, including mild electrolytic condition, environmental benignity and high purity of product. To realize the overall water splitting, efficient electrocatalysts are usually required to reduce the

energy barriers and expedite the sluggish kinetics of the two half reactions, namely, the cathodic hydrogen evolution reaction (HER) and the anodic oxygen evolution reaction (OER) [2,3]. By far, precious metal Pt and IrO₂/RuO₂ are still reckoned as the state-of-the-art electrocatalysts towards the HER and the OER, respectively. [4,5] Nevertheless, their prohibitive price, poor long-term stability and catalytic mono-functionality have severely restricted the large-scale industrialization of the water-splitting technology. To address these issues, it is greatly imperative to develop cost-effective and high-performance nonprecious alternative electrocatalysts, especially, the bifunctional electrocatalysts for both HER and OER in the same electrolyte, to further simplify the electrochemical system and reduce the production cost [6–8]. It is noteworthy that, for practical water electrolysis equipment

* Corresponding author.

** Corresponding author at: Department of Transdisciplinary Studies, Graduate School of Convergence Science and Technology, Seoul National University, 145, Gwanggyo-ro, Yeongtong-gu, Suwon-si, Gyeonggi-do, Republic of Korea.

E-mail addresses: xulin001@njnu.edu.cn (L. Xu), parkat9@snu.ac.kr (Y. Piao).

¹ Theses authors contributed equally to this work

driven by renewable intermittent electricity (e.g., photovoltaic cells, tidal and wind energy), the cell configuration requires the capability to guard against the safety risk occurred at the blending of H₂ and O₂ when power supply fluctuates, especially at low current loads.^[9] Furthermore, in case of frequent power interruptions during cell shutdowns and/or when weather changes, the electrocatalysts usually suffer from depolarization and passivation (or corrosion) caused by the reversed potential and current, leading to the irreversible structural/compositional deterioration and ultimately electrocatalytic deactivation^[10]. These circumstances necessitate a satisfactory and competent bifunctional electrocatalyst to be highly reversible toward HER and OER to meet the practical requirements.

Among a myriad of noble metal-free overall water splitting (OWS) catalysts, transition metal phosphides (TMPs) have emerged as a family of competitive bifunctional candidates due to their cost effectiveness, outstanding mechanical robustness, unique electronic configurations, and high electroactivity^[11,12]. Particularly, the metal-rich TMPs with the molar ratio of M to P ($n_M : n_P > 1$) have garnered considerable attention in virtue of the favorable water adsorption energy, suitable bonding states of reaction intermediates, and pH-universal compatibility for electrolyte^[13]. Nevertheless, the restricted accessibility of exposed surface, inferior conductivity, low intrinsic activity and fabrication difficulties make their overall OWS performance still far from satisfactory^[14]. To circumvent these dilemmas, a range of effective strategies have been proposed to further improve the catalytic performance from the perspectives of electronic modification and nano-architectonics design^[15,16]. Among diverse avenues to electronic modification, the establishment of heterojunctions between different functional components has been extensively documented to be an efficient method to trigger the electron reconfiguration of the adjacent components, regulate the local electronic structures of the active sites, and increase the charge transfer efficiency, leading to the altered chemisorption behaviors of the reaction intermediates, the reduced energy barriers and thus the boosted intrinsic activity^[17–20]. On the other hand, crafting the nanostructures with specific geometrical configurations also provides a powerful approach to augment the accessibility and utilization efficiency of active components and expedite the mass transport, therefore dramatically accelerating the catalytic reaction kinetics^[21]. Architecturally, well-aligned nanoarrays directly grown on the conductive substrates (e.g. Ni foam) as a self-supported electrode are especially advantageous to electrocatalysis due to the excellent electric conductivity, reinforced mechanical strength, enriched channels for electrolyte penetration, sufficient exposure of active sites, and avoidance of the binder involvement for electrode preparation.^[22,23] Last but not least, for gas evolution reaction, the wettability property of the electrode surface also exerts an equally profound impact to determine the electrocatalysis performance^[24]. An ideal electrode surface for electrochemical water splitting requires a strong affinity to aqueous electrolyte, and meanwhile, a rapid release of the generated gas bubbles^[25]. A hydrophilic and aerophobic electrode surface with a low bubble adhesion force could timely repel the accumulation and adhesion of gas bubbles, which effectively avoids the blockage of active sites and ensures the smooth permeation of the electrolyte^[26,27]. It has been well established that the increment of surface roughness helps to construct an aerophobic surface and thus benefit the activity enhancement^[28,29]. Taken together, the rational design of TMP-based heterostructure nanoarrays with a hydrophilic and aerophobic feature is reasonably expected to afford desirable bifunctional performance for efficient OWS.

Bearing the interfacial engineering and wettability manipulation in mind, we herein demonstrate an elaborate design of Ni foam-supported Sn₄P₃/Co₂P “stalk”-“cap”-typed nanoarrays with favorable hydrophilic/aerophobic feature (abbreviated as Sn₄P₃/Co₂P SCNAAs hereafter) as a self-supported bifunctional and reversible electrocatalyst for OWS. The as-fabricated Sn₄P₃/Co₂P SCNAAs exquisitely integrates several prominent advantages for OWS: (1) The abundant Sn₄P₃/Co₂P heterojunctions

imbues the catalyst with optimized local electronic structures of the active sites and increased charge transfer efficiency. (2) The nanoarrayed structure can substantially ensure the sufficient exposure of active sites, remarkable mechanical strength, and promoted mass/electron transport. (3) The grafted “caps” on top of the nanoarrays render the resultant Sn₄P₃/Co₂P SCNAAs with enhanced hydrophilicity and aerophobia, effectively preventing the generated bubbles from accumulation and strong adhesion on the catalyst surface. Consequently, when served as a bifunctional electrocatalyst, the Sn₄P₃/Co₂P SCNAAs exhibit extraordinary electrocatalytic performances in 1.0 M KOH electrolyte, only requiring overpotentials as low as 45.4 and 280.4 mV at 10 mA cm⁻² for HER and OER, respectively, outperforming a vast of the recently reported non-precious electrocatalysts. Moreover, a two-electrode electrolyzer equipped by Sn₄P₃/Co₂P SCNAAs exhibits a cell voltage of 1.56 V at 10 mA cm⁻² with remarkable stability and superior reversibility, which may hold great promises in H₂-associated energy systems.

2. Experimental section

2.1. Reagents

All the reagents were analytical grade and used without further purification. Hydrochloric acid (HCl, 35%), ethanol (EtOH, 99.9%), urea (CH₄N₂O, 99.9%), cobalt nitrate hexahydrate (Co(NO₃)₂·6H₂O, 99.8%), and sodium hypophosphite (NaH₂PO₂, 99.8%) were obtained from Samchun Chemicals (South Korea). Ammonium fluoride (NH₄F, 99.9%), 2-methylimidazole (CH₃C₃H₂N₂H, 99.0%) and sodium stannate trihydrate (Na₂SnO₃·3H₂O, 95.0%) were obtained from Sigma-Aldrich (USA).

2.2. Preparation of Sn₄P₃/Co₂P SCNAAs

The synthesis of Sn₄P₃/Co₂P SCNAAs started from the fabrication of cobalt carbonate hydroxide nanoarrays (denoted CCH) on Ni foam substrate. In a typical synthesis, the cleaned Ni foam was immersed in a mixed aqueous solution of Co(NO₃)₂ (0.09 M), urea (0.285 M) and NH₄F. Then, the reaction precursors were transferred into Teflon-lined stainless steel autoclave and heated at 120 °C for 10 h, generating CCH nanoarrays on Ni foam. Afterwards, the resultant CCH was immersed in 2.0 M 2-methylimidazole solution containing 5 mL of H₂O and 5 mL of EtOH 15 h at room temperature, forming ZIF-67 on the top of CCH nanoneedle arrays (denoted as CCH/ZIF-67). Subsequently, the resultant CCH/ZIF-67 sample was immersed into a 20 mL of 0.002 M Na₂SnO₃ solution, which was transferred to Teflon-lined stainless steel autoclave and kept at 80 °C for 1 h. During this step, the formed CCH/ZIF-67 underwent an ion exchange process between Co²⁺ and Sn⁴⁺, resulting in the formation of Sn-doped CCH/ZIF-67 (denoted Sn-CCH/ZIF-67). Finally, as-obtained Sn-CCH/ZIF-67 and 2.0 g of NaH₂PO₂ were placed in two separate alumina boats with NaH₂PO₂ at the upstream side of the tube furnace. The furnace was maintained at 350 °C for 2 h under Ar flow, generating the Sn₄P₃/Co₂P SCNAAs.

For comparison, a series of reference samples were also prepared according to the above standard protocol, except varying the synthetic parameters. The direct phosphorization treatment of the CCH nanoneedle arrays resulted in the formation of Co₂P nanoarrays (denoted as Co₂P NAs). The phosphorization treatment of CCH/ZIF-67 led to the generation of Co₂P “stalk”-“cap”-typed nanoarrays (referred as Co₂P SCNAAs). The phosphorization treatment of Sn⁴⁺-exchanged CCH nanoneedle arrays brought about Sn₄P₃/Co₂P heterostructured nanoarrays without “caps” (abbreviated as Sn₄P₃/Co₂P NAs).

2.3. Materials characterization

The synthesized materials were characterized by field-emission scanning electron microscope (FE-SEM, Hitachi S-4800), and high

resolution transmission electron microscopy (HRTEM, JEOL JEM-2100 F). X-ray diffraction (XRD) patterns were analysed by a powder X-ray diffractometer (SmartLab, Rigaku, Japan) with a Cu target and a scan rate of $5^\circ \cdot \text{min}^{-1}$. X-ray photoelectron spectroscopy (XPS) analysis was carried out using Axis-HIS spectrometer with Al irradiation of 12 kV and 18 mA.

2.4. Electrochemical measurements

All the electrochemical measurements were conducted on an Autolab workstation (Metrohm, Netherlands) using a three-electrode system in 1.0 M KOH solution (except for the electrochemical water splitting). The active component-decorated Ni foam (1.0 cm² in area, loading mass: 5.22, 5.36, 5.02, and 5.26 mg·cm⁻² for Co₂P NAs, Co₂P SCNAs, Sn₄P₃/Co₂P NAs, and Sn₄P₃/Co₂P SCNAs, respectively) was directly served as a working electrode. The graphite rod and Hg/HgO electrode were used as the counter and reference electrode, respectively. All measured potentials were calibrated to a reversible hydrogen electrode (RHE) according to following equation: $E_{\text{RHE}} = E_{\text{Hg/HgO}} + 0.059 \cdot \text{pH} + 0.140$. The HER and OER tests were performed in N₂- and O₂-saturated 1.0 M KOH electrolyte at a scan rate of 0.5 mV s⁻¹, respectively. The chronopotentiometric measurements for both HER and OER were performed at switched current densities of 10 and 200 mA·cm⁻². The double-layer capacitance (C_{dl}) values of different samples were assessed through the cyclic voltammetry (CV) curves measured from 1.0 V to 1.1 V under various scan rates. The EIS measurements were carried out in the frequency range from 10⁻² to 10⁵ Hz at -0.1 V and 1.60 V for HER and OER respectively. The overall water splitting was performed in a two-electrode system.

3. Result and discussion

3.1. Preparation and characterization

The essential fabrication procedure of the Ni foam-supported Sn₄P₃/Co₂P SCNAs is schematically illustrated in Fig. 1. Firstly, cobalt carbonate hydroxide (Co(CO₃)_{0.5}(OH)_{0.5}, CCH) nanoarrays were directly grown on the commercial Ni foam substrate by a facile hydrothermal method [30]. As revealed by Fig. S1, the CCH nanoneedle arrays are densely and vertically aligned on Ni foam and exhibit length of approximately 8 μm. The resultant CCH nanoarrays were then served as self-sacrificial precursor to provide Co²⁺ ions when immersed into 2-methylimidazole (2-MeIm) ethanol aqueous solution with the aid of solvent and ligand. During this step, 2-MeIm plays a dual role as both an etchant to release Co²⁺ ions from CCH and a ligand for the coordination with Co²⁺ ions to generate ZIF-67. It is noteworthy that the volume ratio of ethanol to water (V_{ethanol}:V_{H2O} = 1:1) renders the solution with the appropriate balance between the dissolution and coordination rate, ensuring the selective nucleation and growth of ZIF-67 on the top of nanoneedle arrays to form a bead-on-string structure, instead of a

core-shell heterostructure.[31,32] As manifested by Fig. S2, ZIF-67 polyhedrons with lateral size of 1–2 μm are grafted on the tips of CCH nanoneedle arrays (denoted as CCH/ZIF-67), taking on an appearance of “cap-on-stalk” structure. It is worth mentioning that the deliberate construction of such “cap-on-stalk” structure is aimed to optimize the wettability feature of the target product, which will be systematically discussed later. Afterwards, the formed CCH/ZIF-67 underwent an ion exchange process between Co²⁺ and Sn⁴⁺ in the presence of Na₂SnO₃, during which the protons generated from the hydrolysis of Na₂SnO₃ may gradually etch the CCH/ZIF-67 and consume the internal Co²⁺ ions, accompanying with the Sn-doping into the CCH/ZIF-67 (referred as Sn-CCH/ZIF-67). The morphological characterization (Fig. S3a) indicates that the nanoarrayed structure can be basically maintained after the Sn modification, but the diameter of the Sn-doped CCH nanoneedles gets thinner than that of the pristine CCH nanoneedles, meanwhile, the overall morphology of the Sn-doped ZIF-67 becomes irregular and the size decreases dramatically as compared with the parent polyhedrons. The X-ray diffraction pattern (XRD, Fig. S3b) suggests that the Sn modification does not introduce any new phase, but causes a slight negative shift of CCH/ZIF-67 diffraction peaks due to the lattice expansion induced by the larger radius of Sn⁴⁺ relative to Co²⁺.[33] Finally, the resultant Sn-CCH/ZIF-67 underwent a low-temperature phosphorization process, during which the released PH₃ gas generated by the thermal decomposition of NaH₂PO₂ would react with Sn-CCH/ZIF-67 to form hetero-structured Sn₄P₃/Co₂P SCNAs.

For comparison, a set of controlled samples, including the single component counterparts with/without “caps” and Sn₄P₃/Co₂P heterostructured nanoarrays without “caps”, were also prepared according to the above standard protocol, excepting adjusting some of the synthetic parameters. The direct phosphorization treatment of the CCH nanoneedle arrays leads to the formation of Co₂P nanoarrays (denoted as Co₂P NAs, Fig. S4). In order to graft “caps” on top of the Co₂P nanoarrays, the formed CCH/ZIF-67 is subjected to a phosphorization process, generating Co₂P “stalk”-“cap”-typed nanoarrays (referred as Co₂P SCNAs, Fig. S5). In addition, Sn₄P₃/Co₂P heterostructured nanoarrays without “caps” (abbreviated as Sn₄P₃/Co₂P NAs, Fig. S6) are also prepared via the phosphorization treatment of the Sn⁴⁺-exchanged CCH nanoneedle arrays.

The panoramic scanning electron microscopy (SEM) image of the as-derived Sn₄P₃/Co₂P SCNAs in Fig. 2a suggests that the surface of the Ni foam substrate is entirely covered by a high density of vertically aligned needle-like nanoarrays. Such 3D nanoarrayed structure can not only effectively promote the mass transfer and electrolyte permeation, but also significantly avoid the agglomeration of active components caused by the large current density or long-term operation during the electrocatalysis process. As revealed by the magnified SEM image (Fig. 2b), the average length and diameter of the “stalks” are measured to be ~8 μm and 150 nm, respectively. Moreover, the topmost “caps” become shapeless as compared with the well-defined parent ZIF-67 polyhedrons after a series of consecutive chemical conversions. A closer observation

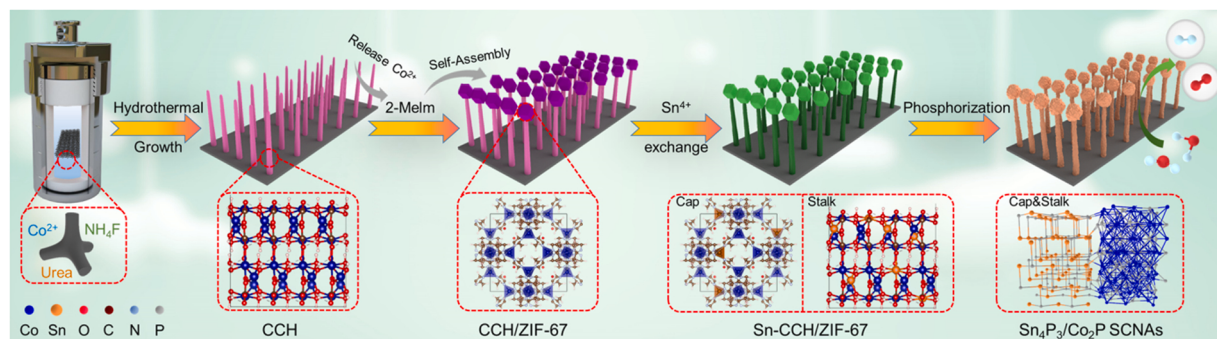


Fig. 1. A schematic illustration for the overall preparation process of Sn₄P₃/Co₂P SCNAs.

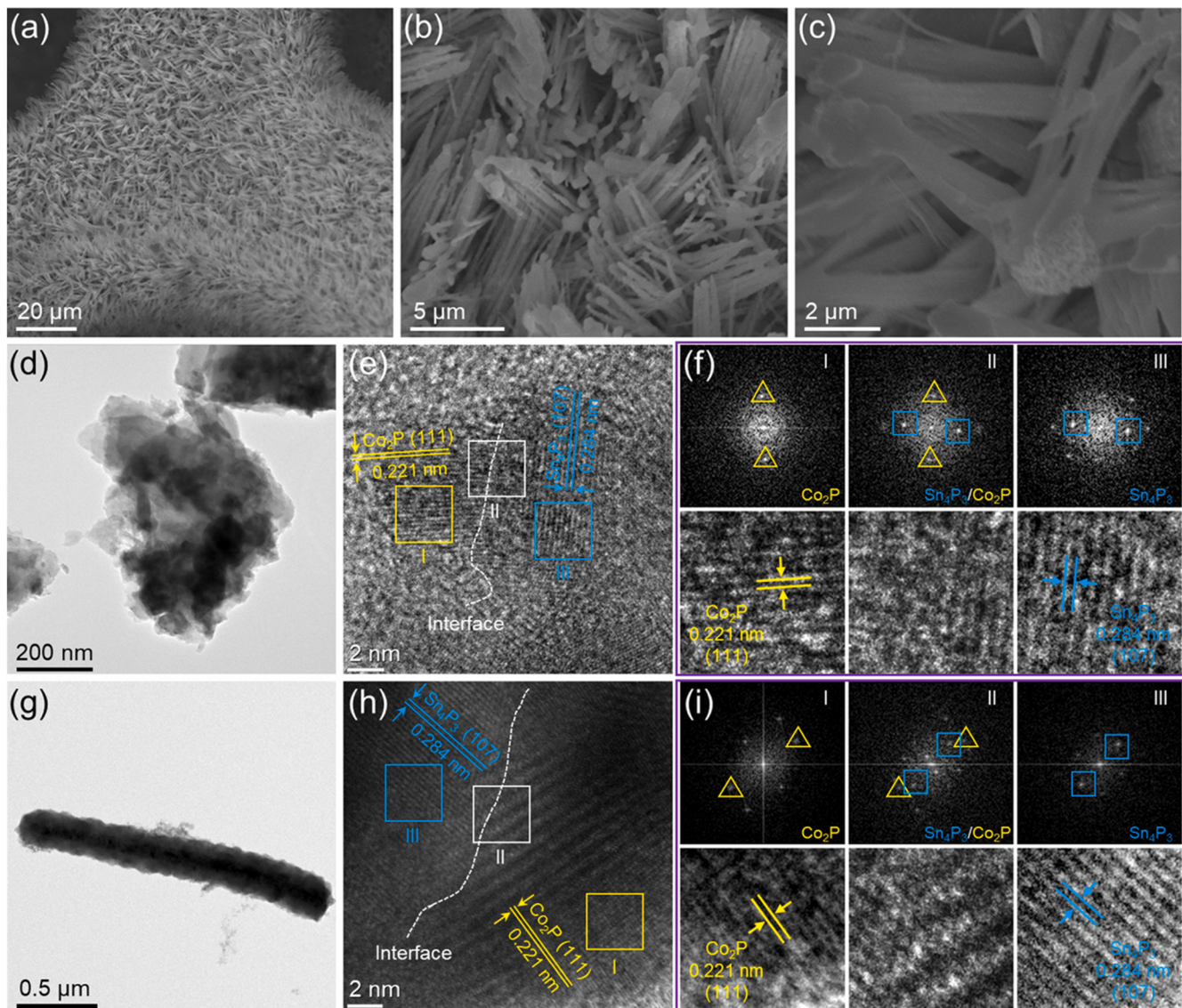


Fig. 2. Morphological characterization of the formed Sn₄P₃/Co₂P SCNAs. (a)-(c) SEM images, (d) TEM image of the “caps”, (e) HRTEM image of the “caps”, (f) FFT patterns and the corresponding HRTEM images of selected areas marked in (e), (g) TEM image of the “stalk”, (h) HRTEM image of the “stalk”, and (i) FFT patterns and the corresponding HRTEM images of selected areas marked in (h).

(Fig. 2c) indicates that the as-derived “caps” with obviously rough surface are intimately grafted on the top of nanoneedles, greatly reinforcing the mechanical strength and modifying the hydrophilic/aerophobic feature of the nanoarrayed electrode. Transmission electron microscopy (TEM) is further used to examine the structural information of the resultant Sn₄P₃/Co₂P NAs. Since the Sn₄P₃/Co₂P SCNAs are tightly grown on the Ni foam substrate, the Sn₄P₃/Co₂P NAs should be scratched from the Ni foam using a steel blade, which may cause the structural damage of Sn₄P₃/Co₂P NAs and lead to the separation of “caps” and “stalks”. Therefore, the TEM images of “caps” and “stalks” are taken separately. The typical TEM image of the Sn₄P₃/Co₂P “caps” (Fig. 2d) verifies their featureless morphology. The high-resolution TEM (HRTEM) image (Fig. 2e) clearly manifests the existence of well-defined heterointerfaces between Sn₄P₃ and Co₂P components, as indicated by the dashed line. The measured lattice fringes with spacings of 0.221 and 0.284 nm are corresponding to the interplanar distances of Co₂P (111) and Sn₄P₃ (107) facets, respectively. Moreover, the fast Fourier transform (FFT) diffraction patterns (Fig. 2f) recorded at Sn₄P₃ and Co₂P adjacent domains further validate the unambiguous formation of heterojunctions between Sn₄P₃ and Co₂P. Likewise, the TEM image

(Fig. 2g), HRTEM image (Fig. 2h) and FFT diffraction patterns (Fig. 2i) of the Sn₄P₃/Co₂P “stalk” collectively demonstrate the hetero-structured feature of the “stalk”. Taken together, it can be inferable that the obtained Sn₄P₃/Co₂P SCNAs are composed of Sn₄P₃/Co₂P heterostructures. The high-angle annular dark-field scanning TEM (HAADF-STEM) images and the elemental mapping analyses (Fig. S7) of the Sn₄P₃/Co₂P “caps” and “stalk” suggest the uniform distribution of Co, Sn, P, and O throughout the entire Sn₄P₃/Co₂P SCNAs.

The heterostructural composition of the as-prepared Sn₄P₃/Co₂P SCNAs was further testified by the XRD pattern (Fig. 3a), which suggests the coexistence of hexagonal Co₂P (JCPDS #54–0413) and rhombohedral Sn₄P₃ (JCPDF #20–1294). It is noteworthy that no diffraction peaks of either CCH or ZIF-67 can be observed, indicating that all cobalt species have been completely transformed into cobalt phosphides during the low-temperature phosphorization process. The surface composition and bonding states of the constituent elements in Sn₄P₃/Co₂P SCNAs were investigated by X-ray photoelectron spectroscopy (XPS) measurements. The survey of spectrum (Fig. 3b) indicates that the surface of Sn₄P₃/Co₂P SCNAs is composed of Co, Sn, P, and O elements. Fig. 3c displays the high-resolution Co 2p spectra of Sn₄P₃/Co₂P SCNAs and

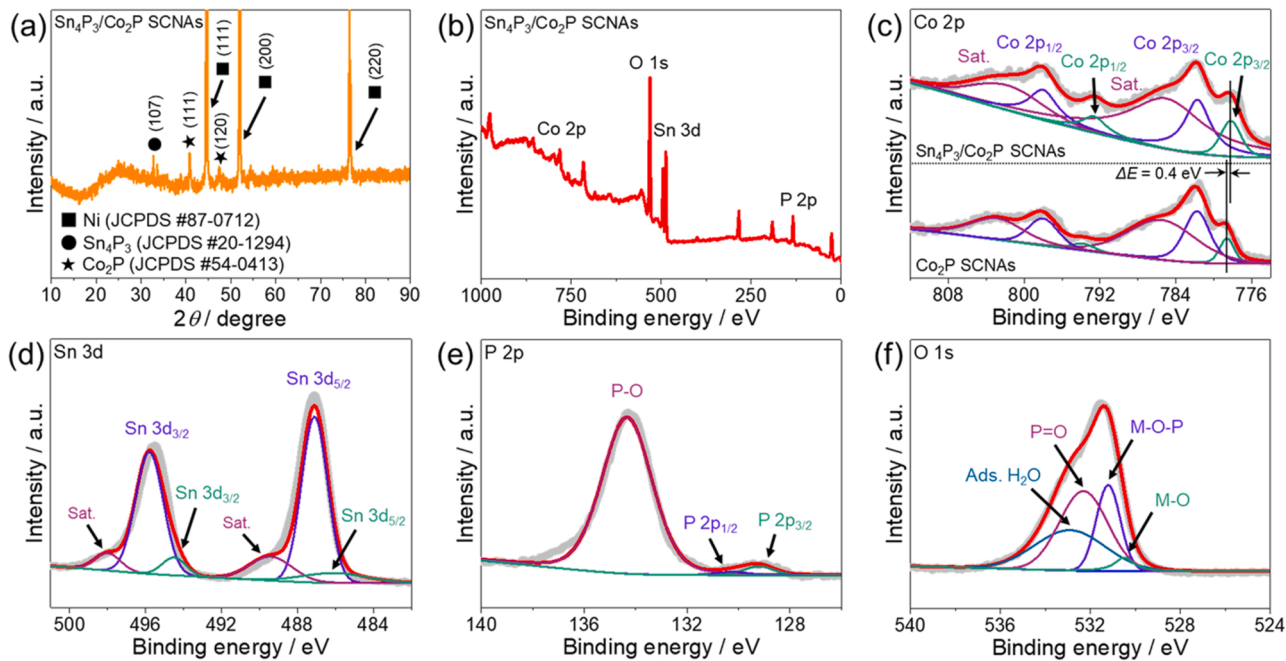


Fig. 3. Compositional analyses of the as-fabricated $\text{Sn}_4\text{P}_3/\text{Co}_2\text{P}$ SCNAs. (a) XRD pattern, (b) XPS survey spectrum, (c) Co 2p spectra of $\text{Sn}_4\text{P}_3/\text{Co}_2\text{P}$ SCNAs and Co_2P SCNAs, (d) Sn 3d spectrum, (e) P 2p spectrum, and (f) O1s spectrum.

Co_2P SCNAs. For the $\text{Sn}_4\text{P}_3/\text{Co}_2\text{P}$ SCNAs, the fitted binding energy peaks appeared at 778.2, 781.7 and 785.3 eV are assigned to Co-P, Co-O and satellite peak of Co 2p_{3/2}, respectively. Additionally, the peaks at 792.6, 798.1 and 802.4 eV are attributed to Co-P, Co-O and satellite peak of Co 2p_{1/2}, respectively [12,34–37]. It is worth noting that binding energies of Co 2p exhibit a negative shift of ~0.4 eV to lower binding energy region as compared with those in Co_2P SCNAs, demonstrating the electronic interactions between Co_2P and Sn_4P_3 moieties caused by the establishment of $\text{Sn}_4\text{P}_3/\text{Co}_2\text{P}$ heterointerfaces [38]. Such modified electronic structure is extensively documented to bring out unique surface reactivity for electrocatalysis. The high-resolution Sn 3d spectrum (Fig. 3d) of $\text{Sn}_4\text{P}_3/\text{Co}_2\text{P}$ SCNAs can be well deconvoluted into two spin-orbit doublets of Sn 3d_{5/2} (485.2 and 487.1 eV) and Sn 3d_{3/2} (494.5 and 495.2 eV) [39–41]. The high-resolution P 2p spectrum (Fig. 3e) suggests the presence of P 2p_{3/2} (129.2 eV) and P 2p_{1/2} (130.2 eV), and oxidized P species/phosphates (134.3 eV) in the formed $\text{Sn}_4\text{P}_3/\text{Co}_2\text{P}$ SCNAs [42,43]. The high-resolution O 1s spectrum (Fig. 3f) can be well fitted into four peaks, which are ascribed to surface adsorbed water (530.5 eV), hydroxy oxygen (531.3 eV), metal-oxide species (532.3 eV), and pyrophosphates (532.9 eV), respectively [44,45].

3.2. Electrochemical performances

3.2.1. Hydrogen evolution reaction (HER) performance

The intimate growth of $\text{Sn}_4\text{P}_3/\text{Co}_2\text{P}$ “stalk”-“cap”-typed nanoarrays with elaborately implanted “caps” and abundant heterojunctions onto Ni foam substrate enables the formed $\text{Sn}_4\text{P}_3/\text{Co}_2\text{P}$ SCNAs to be a promising freestanding bifunctional electrocatalyst for overall water splitting. The HER electrocatalytic performance of the self-supported $\text{Sn}_4\text{P}_3/\text{Co}_2\text{P}$ SCNAs electrode was systematically appraised in N_2 -saturated 1.0 M KOH solution using a typical three-electrode system. In addition, the reference samples, including Ni foam, Co_2P NAs, Co_2P SCNAs, $\text{Sn}_4\text{P}_3/\text{Co}_2\text{P}$ NAs, and commercial Pt/C (20 wt%) catalyst, were also evaluated under the identical test conditions for comparison. All potentials herein have been converted to the reversible hydrogen electrode (RHE) reference. Fig. 4a shows the liner sweep voltammetry (LSV) curves of the tested electrodes. Evidently, the bare Ni foam substrate exhibits an almost negligible HER activity with a weak current density

response even at a considerably large overpotential. For the phosphide-decorated electrodes, the standard $\text{Sn}_4\text{P}_3/\text{Co}_2\text{P}$ SCNAs electrode is identified as the most optimal catalyst among all the phosphide-decorated counterparts. To be specific, to afford a current density of $10 \text{ mA}\cdot\text{cm}^{-2}$ (Fig. 4b), the $\text{Sn}_4\text{P}_3/\text{Co}_2\text{P}$ SCNAs only require a overpotential of 45.4 mV, which is very close to that of commercial Pt/C catalyst (38.7 mV) and drastically lower than those of Co_2P NAs (189.6 mV), Co_2P SCNAs (169.3 mV), and $\text{Sn}_4\text{P}_3/\text{Co}_2\text{P}$ NAs (150.6 mV). Moreover, the $\text{Sn}_4\text{P}_3/\text{Co}_2\text{P}$ SCNAs also exhibit an excellent electrocatalytic behavior at a large current density. At $100 \text{ mA}\cdot\text{cm}^{-2}$, the overpotential occurred on $\text{Sn}_4\text{P}_3/\text{Co}_2\text{P}$ SCNAs is determined to be 120.5 mV, noticeably lower than those of Co_2P NAs (288.6 mV), Co_2P SCNAs (254.3 mV), and $\text{Sn}_4\text{P}_3/\text{Co}_2\text{P}$ NAs (234.7 mV). The HER kinetics is further elucidated by the Tafel slope. A smaller Tafel slope value usually indicates a rapid HER kinetics with efficient electron transport. As inferred from Fig. 4c, the Tafel slope value of $\text{Sn}_4\text{P}_3/\text{Co}_2\text{P}$ SCNAs is calculated to be $72.8 \text{ mV}\cdot\text{dec}^{-1}$, which is significantly smaller than those of Co_2P NAs ($86.8 \text{ mV}\cdot\text{dec}^{-1}$), Co_2P SCNAs ($86.7 \text{ mV}\cdot\text{dec}^{-1}$), and $\text{Sn}_4\text{P}_3/\text{Co}_2\text{P}$ NAs ($84.4 \text{ mV}\cdot\text{dec}^{-1}$). Furthermore, the Tafel slope value of $\text{Sn}_4\text{P}_3/\text{Co}_2\text{P}$ SCNAs also implies that the HER proceeding on $\text{Sn}_4\text{P}_3/\text{Co}_2\text{P}$ SCNAs might follow a Heyrovsky mechanism ($\text{H}_{\text{ads}} + \text{H}_2\text{O} + \text{e}^- \rightarrow \text{H}_2 + \text{OH}^-$). These findings strongly highlight the superiorities of the construction of $\text{Sn}_4\text{P}_3/\text{Co}_2\text{P}$ heterojunctions and the growth of “caps” on top of nanoarrays for the electrocatalytic performance enhancement. The electrochemical impedance spectroscopy (EIS) measurements are performed to further understand the in-depth HER kinetics. As deduced from the Nyquist curves (Fig. S8a), the charge transfer resistance (R_{ct}) of the $\text{Sn}_4\text{P}_3/\text{Co}_2\text{P}$ SCNAs ($R_{\text{ct}} = 2.4 \Omega\cdot\text{cm}^{-2}$) is dramatically lower than that of the single component counterpart (Co_2P SCNAs, $R_{\text{ct}} = 16.6 \Omega\cdot\text{cm}^{-2}$), manifesting that the formation of $\text{Sn}_4\text{P}_3/\text{Co}_2\text{P}$ heterointerfaces enables to promote the charge transfer efficiency and thus accelerate the Faradaic process. Considering the small overpotential and Tafel slope values, the HER activity of the self-supported $\text{Sn}_4\text{P}_3/\text{Co}_2\text{P}$ SCNAs outperforms a vast majority of recently reported precious metal-free electrocatalysts in alkaline media (Table S1). Since the long-term stability is also regarded as a crucial factor to appraise a practical electrocatalyst, the durability of the $\text{Sn}_4\text{P}_3/\text{Co}_2\text{P}$ SCNAs is evaluated by chronopotentiometric measurements at switched current densities of 10 and $200 \text{ mA}\cdot\text{cm}^{-2}$. As shown in

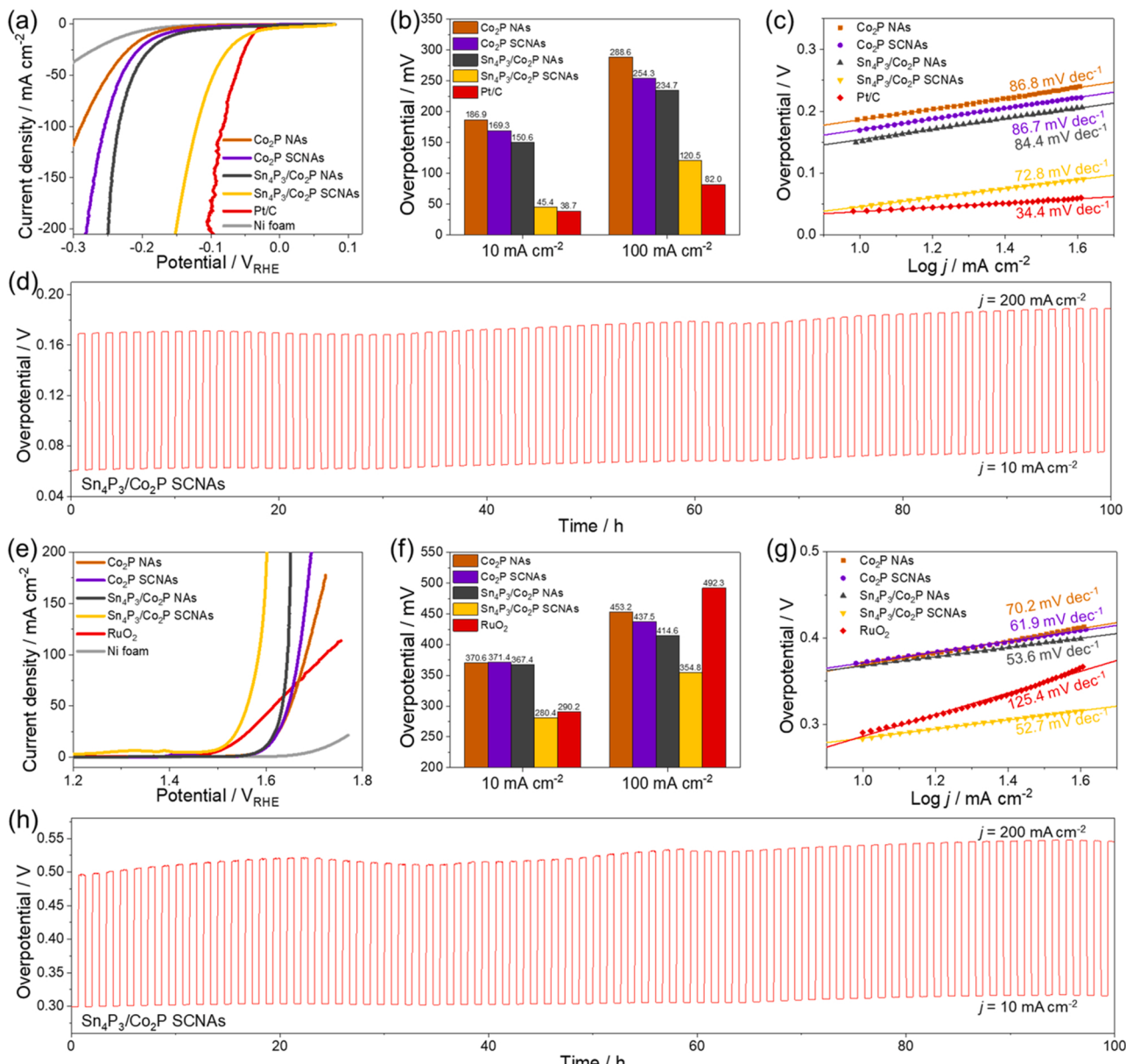


Fig. 4. Electrochemical performance evaluation of as-synthesized Sn₄P₃/Co₂P SCNAs. (a) HER LSV curves of Co₂P NAs, Co₂P SCNAs, Sn₄P₃/Co₂P NAs, Sn₄P₃/Co₂P SCNAs, Pt/C and Ni foam, (b) HER overpotentials of different samples at 10 and 100 mA cm⁻², (c) Tafel plots of different samples, (d) HER chronopotentiometric curve of Sn₄P₃/Co₂P SCNAs at 10 and 200 mA·cm⁻² for 100 h. (e) OER LSV curves of Co₂P NAs, Co₂P SCNAs, Sn₄P₃/Co₂P NAs, Sn₄P₃/Co₂P SCNAs, RuO₂ and Ni foam, (f) OER overpotentials of different samples at 10 and 100 mA cm⁻², (g) Tafel plots of different samples, (h) OER chronopotentiometric curve of Sn₄P₃/Co₂P SCNAs at 10 and 200 mA·cm⁻² for 100 h.

Fig. 4d, the Sn₄P₃/Co₂P SCNAs electrode could almost maintain its original performance without noticeable increase of overpotential even after 100 h, demonstrating its excellent electrochemical stability. The HRTEM images (Fig. S9) of the “stalk” and “caps” for the post-HER Sn₄P₃/Co₂P SCNAs clearly demonstrate that the Sn₄P₃/Co₂P heterojunctions could well preserved after the HER test, testifying the salient structural robustness of the Sn₄P₃/Co₂P SCNAs catalyst.

3.2.2. Oxygen evolution reaction (OER) performance

The OER performance of freestanding Sn₄P₃/Co₂P SCNAs electrode was also investigated in O₂-saturated 1.0 M KOH electrolyte. For comparison, commercial RuO₂ catalyst was also used as a benchmark under the identical condition. The OER LSV polarization curves (Fig. 4e) of different samples indicate that the Sn₄P₃/Co₂P SCNAs exhibit the highest OER activity. As listed in Fig. 4f, the Sn₄P₃/Co₂P SCNAs display

the lowest overpotential of 280.4 mV at 10 mA cm⁻², whereas Co₂P NAs, Co₂P SCNAs, Sn₄P₃/Co₂P NAs and RuO₂ require considerably larger overpotentials of 370.6, 371.4, 367.4, and 290.2 mV, respectively. Moreover, the anodic OER current of the Sn₄P₃/Co₂P SCNAs rises promptly as the potential increases, requiring to the lowest overpotential at a large current density. For instance, the Sn₄P₃/Co₂P SCNAs need an overpotential of 354.8 mV to achieve a current density of 100 mA·cm⁻², significantly smaller than those of Co₂P NAs (453.2 mV), Co₂P SCNAs (437.5 mV), Sn₄P₃/Co₂P NAs (414.6 mV), and RuO₂ (492.3 mV). Fig. 4g shows that the Tafel slope of 52.7 mV·dec⁻¹ for Sn₄P₃/Co₂P SCNAs is much smaller than those of Co₂P NAs (70.2 mV·dec⁻¹), Co₂P SCNAs (61.9 mV·dec⁻¹), Sn₄P₃/Co₂P NAs (53.6 mV·dec⁻¹) and even lower than that of the RuO₂ catalyst (125.4 mV·dec⁻¹), again suggesting the favorable OER kinetics of the formed Sn₄P₃/Co₂P SCNAs. Notably, the OER activity of Sn₄P₃/Co₂P

SCNAs also overmatches most of the recently reported nonprecious metal-based electrocatalysts (Table S2). The comparison of Nyquist plots (Fig. S8b) of $\text{Sn}_4\text{P}_3/\text{Co}_2\text{P}$ SCNAAs and Co_2P SCNAAs further proves that the establishment of $\text{Sn}_4\text{P}_3/\text{Co}_2\text{P}$ heterojunctions is conducive to reduce the charge transfer resistance and thus facilitate the charge transfer. To further unravel the origin of the excellent electrocatalytic activity of $\text{Sn}_4\text{P}_3/\text{Co}_2\text{P}$ SCNAAs, the electrochemical double-layer capacitance (C_{dl}) values of different electrocatalysts, which are linearly related to their electrochemical active surface areas (ECSAs), are estimated according to the cyclic voltammograms (CVs) performed within non-Faradaic potential region at various scan rates (Fig. S10). The $\text{Sn}_4\text{P}_3/\text{Co}_2\text{P}$ SCNAAs exhibit the C_{dl} value of $65.6 \text{ mF}\cdot\text{cm}^{-2}$, which is greatly higher than those of Co_2P NAs ($29.0 \text{ mF}\cdot\text{cm}^{-2}$), Co_2P SCNAAs ($46.2 \text{ mF}\cdot\text{cm}^{-2}$), and $\text{Sn}_4\text{P}_3/\text{Co}_2\text{P}$ NAs ($53.4 \text{ mF}\cdot\text{cm}^{-2}$), signifying that the formation of $\text{Sn}_4\text{P}_3/\text{Co}_2\text{P}$ heterojunctions can also enormously create more active sites and therefore boost the electrocatalytic activity. In

addition, the ECSA-normalized LSV curves (Fig. S11) demonstrate the highest intrinsic electrocatalytic activity of the built $\text{Sn}_4\text{P}_3/\text{Co}_2\text{P}$ heterojunctions. During the long-term stability test (Fig. 4h), the $\text{Sn}_4\text{P}_3/\text{Co}_2\text{P}$ SCNAAs could still preserve the original activity without appreciable degradation after 100 h of continuous operation at switched current densities of 10 and $200 \text{ mA}\cdot\text{cm}^{-2}$, reflecting its superior electrochemical robustness. The HRTEM images (Fig. S12) of the “stalk” and “caps” for the post-OER $\text{Sn}_4\text{P}_3/\text{Co}_2\text{P}$ SCNAAs indicate the in situ generation of a thin layer of CoOOH species after the OER test, which might serve as the actual active sites for OER.

3.2.3. Bifunctional activity towards OWS

Motivated by the outstanding HER and OER electrochemical properties of the as-synthesized $\text{Sn}_4\text{P}_3/\text{Co}_2\text{P}$ SCNAAs, a two-electrode electrolyzer by directly using the freestanding $\text{Sn}_4\text{P}_3/\text{Co}_2\text{P}$ SCNAAs as both cathode and anode was equipped for OWS in 1.0 M KOH electrolyte

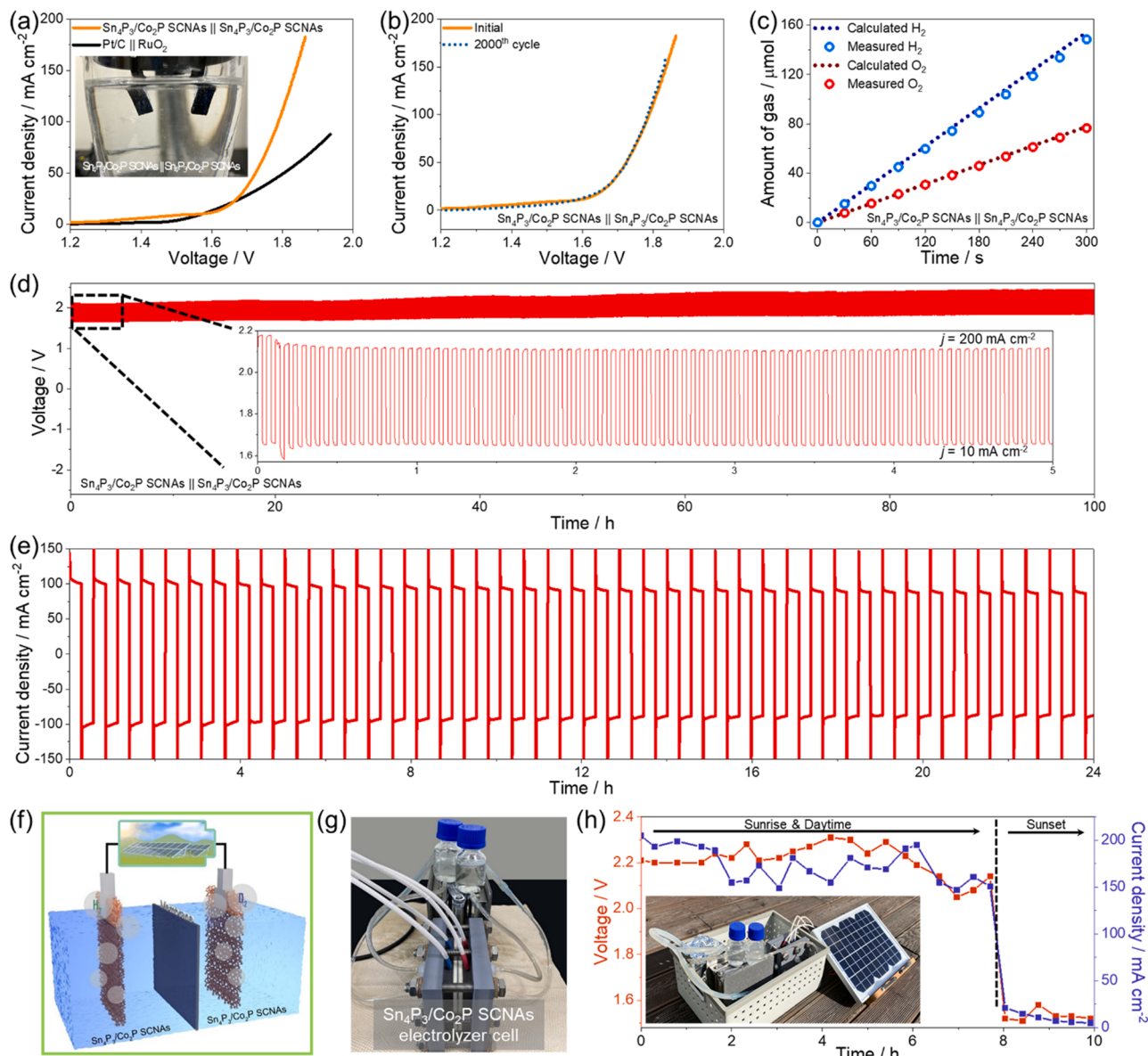


Fig. 5. Overall water splitting performance of $\text{Sn}_4\text{P}_3/\text{Co}_2\text{P}$ SCNAAs-built two-electrode cell. (a) Water splitting LSV curves of $\text{Sn}_4\text{P}_3/\text{Co}_2\text{P}$ SCNAAs-built cell and $\text{Pt}/\text{C}||\text{RuO}_2$ -based cell, inset: the digital photo of $\text{Sn}_4\text{P}_3/\text{Co}_2\text{P}$ SCNAAs-built cell, (b) LSV polarization curves of the $\text{Sn}_4\text{P}_3/\text{Co}_2\text{P}$ SCNAAs-built cell before and after 2000 cycles, (c) experimental and theoretical amounts of H_2 and O_2 during water splitting, (d) chronopotentiometric curve of $\text{Sn}_4\text{P}_3/\text{Co}_2\text{P}$ SCNAAs-cell at 10 and $200 \text{ mA}\cdot\text{cm}^{-2}$ for 100 h. (e) chronoamperometric curve of $\text{Sn}_4\text{P}_3/\text{Co}_2\text{P}$ SCNAAs-built cell with the applied potential of 1.8 V and the polarity switch interval of 1000 s for 24 h, (f) the schematic illustration of the two-electrode electrolyzer, (g) a digital photo of the assembled electrolyzer, (h) the voltage and current response of the solar-driven $\text{Sn}_4\text{P}_3/\text{Co}_2\text{P}$ SCNAAs-cell for water splitting, inset: the digital photo of the solar-driven $\text{Sn}_4\text{P}_3/\text{Co}_2\text{P}$ SCNAAs-cell.

($\text{Sn}_4\text{P}_3/\text{Co}_2\text{P}$ SCNAs|| $\text{Sn}_4\text{P}_3/\text{Co}_2\text{P}$ SCNAs, inset of Fig. 5a). For comparison, the state-of-the-art counterpart using Pt/C and RuO₂ as cathode and anode, respectively, was also assembled (Pt/C||RuO₂). As presented by the OWS LSV polarization curves (Fig. 5a), the $\text{Sn}_4\text{P}_3/\text{Co}_2\text{P}$ SCNAs|| $\text{Sn}_4\text{P}_3/\text{Co}_2\text{P}$ SCNAs-assembled electrolytic cell only requires a cell voltage of 1.56 V to afford a current density of 10 mA cm^{-2} , which is lower than that of Pt/C||RuO₂ benchmark (1.57 V). More impressively, the current density of $\text{Sn}_4\text{P}_3/\text{Co}_2\text{P}$ SCNAs-based cell rises steeply as the applied voltage increases, resulting in the low cell voltages at higher current densities. For instance, the applied voltage of the $\text{Sn}_4\text{P}_3/\text{Co}_2\text{P}$ SCNAs-based cell at 80 mA cm^{-2} is determined to be 1.72 V, enormously lower than that of the Pt/C||RuO₂ reference (1.91 V). This distinct comparison indicates that the $\text{Sn}_4\text{P}_3/\text{Co}_2\text{P}$ SCNAs-built cell is more energy saving and exhibits higher energy conversion efficiency from electricity to chemical energy in practical devices. As displayed in Fig. 5b, the LSV curve of the $\text{Sn}_4\text{P}_3/\text{Co}_2\text{P}$ SCNAs-based cell after 2000 CV cycles almost keeps overlapped with the initial one, demonstrating the excellent stability for electrochemical water splitting. Moreover, the SEM image (Fig. S13) of the $\text{Sn}_4\text{P}_3/\text{Co}_2\text{P}$ SCNAs suggests that the nanoarrayed structure can be well maintained after the stability test, indicating the superior structural robustness of the $\text{Sn}_4\text{P}_3/\text{Co}_2\text{P}$ SCNAs. The OWS faradaic efficiency of the $\text{Sn}_4\text{P}_3/\text{Co}_2\text{P}$ SCNAs-equipped cell is identified by measuring the amounts of generated H₂ and O₂ using a water drainage method. As reflected by Fig. 5c, the experimental gas amount-time curves of H₂ and O₂ exhibit a perfect linear relationship and almost keep identical with the theoretical ones. Moreover, the measured amount ratio of H₂ to O₂ is approximately to be 2: 1, suggesting a nearly 100% Faradaic efficiency of the OWS process. The long-term chronopotentiometric curve (Fig. 5d) obtained at switched current densities of 10 and 200 mA cm^{-2} indicates that the cell voltages remain quite stable without noticeable increment at either moderate or vigorous electrolysis condition even after 100 h, further testifying the extraordinary OWS stability of the $\text{Sn}_4\text{P}_3/\text{Co}_2\text{P}$ SCNAs.

Notably, for water electrolysis devices powered by intermittent renewable energy resources (e.g., photovoltaic cells and wind), the frequent power interruptions will inevitably cause the electrode depolarization and reversed bias on the electrode surface, which may ultimately lead to the electrode corrosion and electrocatalytic performance degradation. Therefore, it is greatly imperative to develop bifunctional switchable electrocatalysts with excellent reversibility for practical water splitting. Herein, the reversibility of the $\text{Sn}_4\text{P}_3/\text{Co}_2\text{P}$ SCNAs was also evaluated by frequently switching the electrode polarity to investigate their practicability. Fig. 5e shows the current density-time curve recorded at the periodically reversed applied potential from 1.8 to -1.8 V with every interval of 1000 s. Apparently, the $\text{Sn}_4\text{P}_3/\text{Co}_2\text{P}$ SCNAs-equipped cell exhibits an outstanding stability and prompt response upon the frequent changes of the electrode polarity. The current density could basically stabilize at $\sim 100 \text{ mA cm}^{-2}$ for both HER and OER without any appreciable hysteresis for over 24 h, reflecting the extraordinary reversibility and superior robustness of the $\text{Sn}_4\text{P}_3/\text{Co}_2\text{P}$ SCNAs to withstand the power supply fluctuations. To further promote the potentiality for practical applications, the $\text{Sn}_4\text{P}_3/\text{Co}_2\text{P}$ SCNAs were further assembled into an H-typed electrolyzer separated with a membrane, which was driven by a commercial solar cell (Fig. 5f and g). Fig. 5h records the dynamic OWS process powered by the solar panel. When the solar cell is utilized as the power source at daytime, the voltage generated by this solar cell is around 2.2 V, which could deliver a relatively stable current density of 175 mA cm^{-2} . Whereas, the voltage of the solar cell after the sunset is too low to trigger the water splitting. Undoubtedly, the above findings again manifest the practical potentiality of the well-designed $\text{Sn}_4\text{P}_3/\text{Co}_2\text{P}$ SCNAs for large-scale water electrolysis applications.

3.3. Wettability and gas behavior analysis

The prominent HER and OER performances of the as-fabricated

$\text{Sn}_4\text{P}_3/\text{Co}_2\text{P}$ SCNAs can be attributed to the favorable composition and well-designed micro/nano-architecture. Firstly, the formation of $\text{Sn}_4\text{P}_3/\text{Co}_2\text{P}$ intimate nanointerfaces could significantly modulate the electronic structures of the constituent components, which may induce the rapid charge transfer efficiency, the optimized reaction pathways for HER and OER, and thus the boosted intrinsic activity. Secondly, the needle-like nanoarrays could effectively enlarge the exposure of active sites, shorten the mass diffusion distance, and promote the electrolyte permeation, resulting in the dramatically enhanced reaction kinetics. Moreover, the Ni foam substrate, featuring with remarkable conductivity and hierarchically porous network, not only offers efficient electron transfer highways, but also tightly stabilizes the active components and greatly enhance the mechanical strength. Furthermore, the free-standing electrode configuration could effectively circumvent the polymeric binder-induced issues, such as undesirable dead volume/mass and increased electric resistance. Thirdly, the purposely implanted “caps” on top of the nanoarrays may significantly increase the surface roughness, and thus affect the surface wettability and gas bubble releasing behavior during the electrochemical water splitting process. To validate this viewpoint, the surface wettability of different electrodes was examined by contact-angle measurements. As shown in Fig. 6a, by comparing the contact angles of Co₂P NAs, Co₂P SCNAs, Sn₄P₃/Co₂P NAs, and Sn₄P₃/Co₂P SCNAs, it is deduced that the electrode surface becomes more hydrophilic upon the implantation of the rough “caps”. Furthermore, a camera was utilized to record the OER process to compare the size distribution and detachment behavior of the generated O₂ bubbles on different electrodes at a current density of 150 mA cm^{-2} . Generally speaking, the gas bubbles with larger diameter will result in the blocked electrode surface area and the greater detachment force from the electrode surface, leading to the enlarged diffusion resistance and increased overpotential during the electrocatalysis process. As observed from the bubble size distribution histogram (Fig. 6b-e), the O₂ bubbles released from Sn₄P₃/Co₂P SCNAs ($\sim 59 \mu\text{m}$) are distinctly smaller than those escaped from Co₂P NAs ($\sim 81 \mu\text{m}$), Co₂P SCNAs ($\sim 71 \mu\text{m}$), and Sn₄P₃/Co₂P NAs ($\sim 77 \mu\text{m}$), suggesting the more aerophobic feature and easy gas bubbles departure of the standard Sn₄P₃/Co₂P SCNAs. The above findings manifest that the grafted “caps” on top of the nanoarrays endow the formed Sn₄P₃/Co₂P SCNAs with increased hydrophilicity and aerophobicity, effectively preventing the generated bubbles from accumulation and strong adhesion on the catalyst surface, as schematically illustrated in Fig. 6f. All in all, the heterojunction synergy and hydrophilic/aerophobic nanoarrayed architecture enable the well-designed Sn₄P₃/Co₂P SCNAs as an economical and efficient bifunctional electrocatalyst for water splitting.

4. Conclusions

In summary, we have reported the fabrication of Ni foam-supported Sn₄P₃/Co₂P “stalk”-“cap”-typed nanoarrays with favorable hydrophilic/aerophobic rough “caps” as a freestanding bifunctional electrocatalyst for overall water splitting. The delicate establishment of Sn₄P₃/Co₂P heterojunctions and construction of “stalk”-“cap”-typed nanoarrays endow the as-prepared Sn₄P₃/Co₂P SCNAs with regulated electronic structure, rapid charge transfer efficiency, optimized reaction pathways and increased active sites. Moreover, the hydrophilic and aerophobic features are beneficial for the electrolyte permeation and rapid departure of evolved gas bubbles, which can significantly expedite mass transfer. Due to the above compositional synergy and architectural advantages, when served as a bifunctional electrocatalyst, the Sn₄P₃/Co₂P SCNAs display excellent electrocatalytic performance in 1.0 M KOH medium, requiring overpotentials of 45.4 and 280.4 mV at 10 mA cm^{-2} for HER and OER, respectively, exceeding a majority of the recently reported noble metal-free electrocatalysts. Furthermore, a two-electrode electrolyzer assembled by Sn₄P₃/Co₂P SCNAs exhibits a cell voltage of 1.56 V at 10 mA cm^{-2} with remarkable stability and extraordinary reversibility, representing an affordable and efficient bifunctional

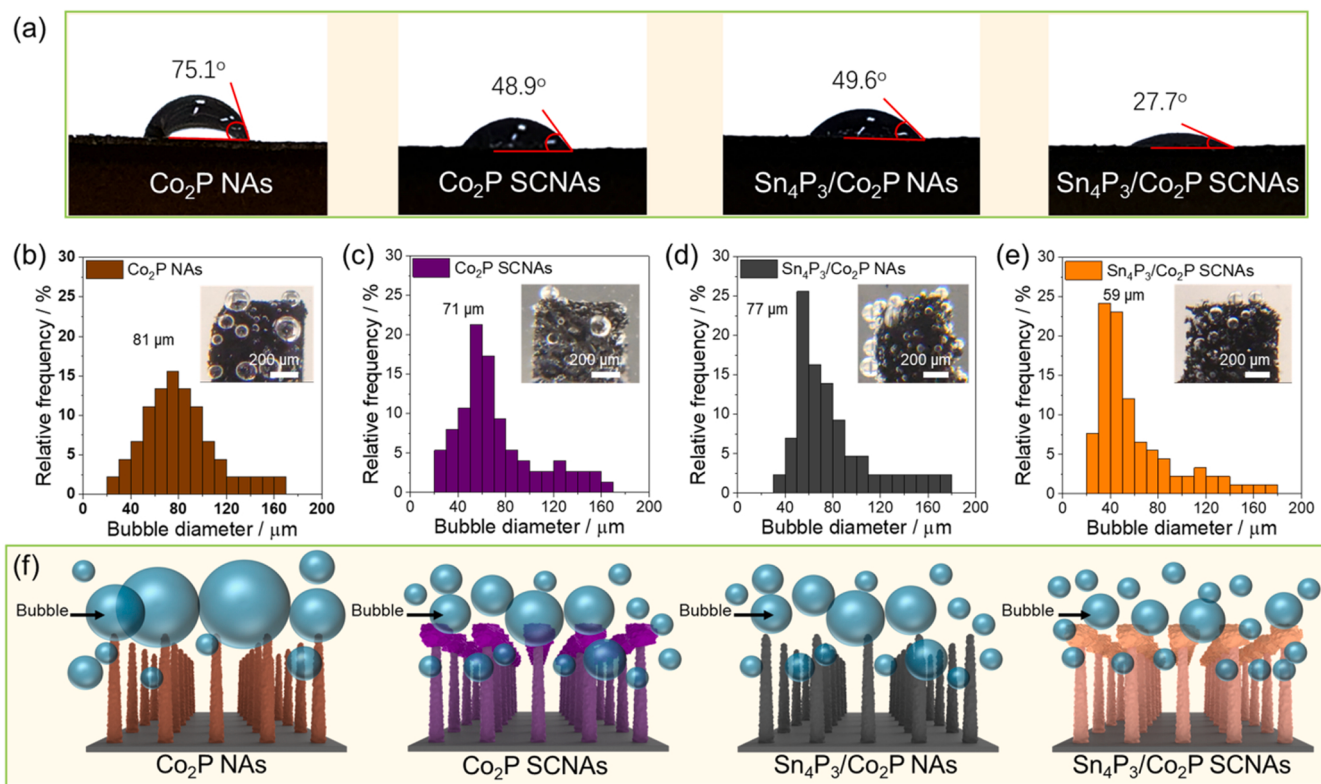


Fig. 6. (a) Contact angle measurements of Co₂P NAs, Co₂P SCNAs, Sn₄P₃/Co₂P NAs, and Sn₄P₃/Co₂P SCNAs, the average gas bubble diameter generated on (b) Co₂P NAs, (c) Co₂P SCNAs, (d) Sn₄P₃/Co₂P NAs, and (e) Sn₄P₃/Co₂P SCNAs, and (f) the schematic illustration of bubble size release from different electrodes.

electrocatalyst for diverse H₂-associated energy devices. We believe that the concept of interface engineering and surface wettability tuning highlighted in this study may inspire the future design of cost-effectiveness and high-efficiency electrocatalysts for plenty of renewable energy systems.

CRediT authorship contribution statement

Xinyu Qin: Conceptualization, Investigation, Data curation, Formal analysis, Writing – original draft. **Bingyi Yan:** Methodology, Investigation, Data curation, Formal analysis. **Dongwon Kim:** Investigation, Data curation, Formal analysis. **Zhishun Teng:** Data curation, Formal analysis. **Tianyu Chen:** Data curation. **Juhhyung Choi:** Data curation. **Lin Xu:** Conceptualization, Supervision, Writing – original draft, Writing– review & editing. **Yuanzhe Piao:** Supervision, Resources, Project administration, Funding acquisition, Writing – review & editing.

Declaration of Competing Interest

The authors declare that they have no known competing financial interests or personal relationships that could have appeared to influence the work reported in this paper.

Acknowledgements

This research was supported by the Basic Science Research Program through the National Research Foundation of Korea (NRF) funded by the Ministry of Education (NRF-2018R1D1A1B07051249), Nano Material Technology Development Program (NRF-2015M3A7B6027970) and Science and Technology Amicable Relationships (STAR) Program (NRF-2019K1A3A1A21031052) of MSIT/NRF. This research was also supported by the Center for Integrated Smart Sensors funded by the Ministry of Science, ICT and Future Planning, Republic of Korea, as Global Frontier Project (CIS-2012M3A6A6054186). The authors wish to thank

the National Center for Inter-University Research Facilities (NCIRF), and the Research Institute of Advanced Materials (RIAM) at Seoul National University for using the research facilities.

Appendix A. Supporting information

Supplementary data associated with this article can be found in the online version at doi:10.1016/j.apcatb.2021.120923.

References

- [1] Y. Jiao, Y. Zheng, M. Jaroniec, S.Z. Qiao, Design of electrocatalysts for oxygen- and hydrogen-involved energy conversion reactions, *Chem. Soc. Rev.* 44 (2015) 2060–2086, <https://doi.org/10.1039/c4cs00470a>.
- [2] D.Y. Chung, S.K. Park, Y.H. Chung, S.H. Yu, D.H. Lim, N. Jung, H.C. Ham, H.Y. Park, Y. Piao, S.J. Yoo, Y.E. Sung, Edge-exposed MoS₂ nano-assembled structures as efficient electrocatalysts for hydrogen evolution reaction, *Nanoscale* 6 (2014) 2131–2136, <https://doi.org/10.1039/c3nr05228a>.
- [3] J. Kibsgaard, I. Chorkendorff, Considerations for the scaling-up of water splitting catalysts, *Nat. Energy* 4 (2019) 430–433, <https://doi.org/10.1038/s41560-019-0407-1>.
- [4] Q. Wu, Q. Gao, L. Sun, H. Guo, X. Tai, D. Li, L. Liu, C. Ling, X. Sun, Facilitating active species by decorating CeO₂ on Ni₃S₂ nanosheets for efficient water oxidation electrocatalysis, *Chin. J. Catal.* 42 (2021) 482–489, [https://doi.org/10.1016/s1872-2067\(20\)63663-4](https://doi.org/10.1016/s1872-2067(20)63663-4).
- [5] S.S. Wang, L. Jiao, Y. Qian, W.C. Hu, G.Y. Xu, C. Wang, H.L. Jiang, Boosting electrocatalytic hydrogen evolution over metal-organic frameworks by plasmon-induced hot-electron injection, *Angew. Chem. Int. Ed.* 58 (2019) 10713–10717, <https://doi.org/10.1002/anie.201906134>.
- [6] G. Zhou, M. Li, Y. Li, H. Dong, D. Sun, X. Liu, L. Xu, Z. Tian, Y. Tang, Regulating the electronic structure of CoP nanosheets by O incorporation for high-efficiency electrochemical overall water splitting, *Adv. Funct. Mater.* 30 (2019), 1905252, <https://doi.org/10.1002/adfm.201905252>.
- [7] J. Choi, D. Kim, W. Zheng, B. Yan, Y. Li, L.Y.S. Lee, Y. Piao, Interface engineered NiFe₂O_{4-x}/NiMoO₄ nanowire arrays for electrochemical oxygen evolution, *Appl. Catal. B* 286 (2021), 119857, <https://doi.org/10.1016/j.apcatb.2020.119857>.
- [8] L. Jiao, Y.X. Zhou, H.L. Jiang, Metal-organic framework-based CoP/reduced graphene oxide: high-performance bifunctional electrocatalyst for overall water splitting, *Chem. Sci.* 7 (2016) 1690–1695, <https://doi.org/10.1039/c5sc04425a>.

[9] Q. Zhang, N.M. Bedford, J. Pan, X. Lu, R. Amal, A. Fully Reversible Water, Electrolyzer cell made up from FeCoNi(Oxy)hydroxide atomic layers, *Adv. Energy Mater.* 9 (2019), 1901312, <https://doi.org/10.1002/aenm.201901312>.

[10] M. Gong, H. Dai, A mini review of NiFe-based materials as highly active oxygen evolution reaction electrocatalysts, *Nano Res* 8 (2014) 23–39, <https://doi.org/10.1007/s12274-014-0591-z>.

[11] S. Carenco, D. Portehault, C. Boissiere, N. Mezailles, C. Sanchez, Nanoscaled metal borides and phosphides: recent developments and perspectives, *Chem. Rev.* 113 (2013) 7981–8065, <https://doi.org/10.1021/cr400020d>.

[12] Z. Jin, P. Li, D. Xiao, Metallic Co₂P ultrathin nanowires distinguished from CoP as robust electrocatalysts for overall water-splitting, *Green Chem.* 18 (2016) 1459–1464, <https://doi.org/10.1039/c5gc02462e>.

[13] A. Ray, S. Sultana, L. Paramanik, K.M. Parida, Recent advances in phase, size, and morphology-oriented nanostructured nickel phosphide for overall water splitting, *J. Mater. Chem. A* 8 (2020) 19196–19245, <https://doi.org/10.1039/dta05797e>.

[14] C. Huang, L. Yu, W. Zhang, Q. Xiao, J. Zhou, Y. Zhang, P. An, J. Zhang, Y. Yu, N-doped Ni-Mo based sulfides for high-efficiency and stable hydrogen evolution reaction, *Appl. Catal. B* 276 (2020), 119137, <https://doi.org/10.1016/j.apcatb.2020.119137>.

[15] Heterojunction catalyst in electrocatalytic water splitting, in: Z. Li, M. Hu, P. Wang, J. Liu, J. Yao, C. Li (Eds.), *Coord. Chem. Rev.*, 439, 2021, 213953, <https://doi.org/10.1016/j.ccr.2021.213953>.

[16] M. Wang, W. Fu, L. Du, Y. Wei, P. Rao, L. Wei, X. Zhao, Y. Wang, S. Sun, Surface engineering by doping manganese into cobalt phosphide towards highly efficient bifunctional HER and OER electrocatalysis, *Appl. Surf. Sci.* 515 (2020), 146059, <https://doi.org/10.1016/j.apsusc.2020.146059>.

[17] R. Boppella, J. Tan, W. Yang, J. Moon, Homologous CoP/NiCoP heterostructure on N-doped carbon for highly efficient and pH-universal hydrogen evolution electrocatalysis, *Adv. Funct. Mater.* 29 (2018), 1807976, <https://doi.org/10.1002/adfm.201807976>.

[18] M.S. Faber, R. Dziedzic, M.A. Lukowski, N.S. Kaiser, Q. Ding, S. Jin, High-performance electrocatalysis using metallic cobalt pyrite (CoS₍₂₎) micro- and nanostructures, *J. Am. Chem. Soc.* 136 (2014) 10053–10061, <https://doi.org/10.1021/ja504099w>.

[19] X. Luo, P. Ji, P. Wang, R. Cheng, D. Chen, C. Lin, J. Zhang, J. He, Z. Shi, N. Li, S. Xiao, S. Mu, Interface engineering of hierarchical branched Mo-doped Ni₃S₂/Ni_xP_y hollow heterostructure nanorods for efficient overall water splitting, *Adv. Energy Mater.* 10 (2020), 1903891, <https://doi.org/10.1002/aenm.201903891>.

[20] M. Liu, K.A. Min, B. Han, L.Y.S. Lee, Interfacing or doping? Role of Ce in highly promoted water oxidation of NiFe-layered double hydroxide, *Adv. Energy Mater.* 11 (2021), 2101281, <https://doi.org/10.1002/aenm.202101281>.

[21] M.I. Jamesh, Y. Kuang, X. Sun, Constructing earth-abundant 3D nanoarrays for efficient overall water splitting - a review, *ChemCatChem* 11 (2019) 1550–1575, <https://doi.org/10.1002/cctc.201801783>.

[22] W. Yuan, M. Zhao, J. Yuan, C.M. Li, Ni foam supported three-dimensional vertically aligned and networked layered CoO nanosheet/graphene hybrid array as a high-performance oxygen evolution electrode, *J. Power Sources* 319 (2016) 159–167, <https://doi.org/10.1016/j.jpowsour.2016.04.044>.

[23] W. Chen, J. Fang, Y. Zhang, G. Chen, S. Zhao, R. Huang, Y. Zhou, Morphological and structure dual modulation of cobalt-based layer double hydroxides by Ni doping and 2-methylimidazole inducing a bifunctional electrocatalysts for overall water splitting, *J. Power Sources* 400 (2018) 172–182, <https://doi.org/10.1016/j.jpowsour.2018.08.023>.

[24] Y.T. Xu, X. Xiao, Z.M. Ye, S. Zhao, R. Shen, C.T. He, J.P. Zhang, Y. Li, X.M. Chen, Cage-confinement pyrolysis route to ultrasmall tungsten carbide nanoparticles for efficient electrocatalytic hydrogen evolution, *J. Am. Chem. Soc.* 139 (2017) 5285–5288, <https://doi.org/10.1021/jacs.7b00165>.

[25] R. Xu, R. Wu, Y. Shi, J. Zhang, B. Zhang, Ni₃Se₂ nanoforest/Ni foam as a hydrophilic, metallic, and self-supported bifunctional electrocatalyst for both H₂ and O₂ generations, *Nano Energy* 24 (2016) 103–110, <https://doi.org/10.1016/j.nanoen.2016.04.006>.

[26] Y. Huang, L. Liu, X. Liu, Modulated electrochemical oxygen evolution catalyzed by MoS₂ nanoflakes from atomic layer deposition, *Nat. Nanotechnol.* 30 (2019), 095402, <https://doi.org/10.1088/1361-6528/aaef13>.

[27] M. Yu, Z. Wang, J. Liu, F. Sun, P. Yang, J. Qiu, A hierarchically porous and hydrophilic 3D nickel-iron/MXene electrode for accelerating oxygen and hydrogen evolution at high current densities, *Nano Energy* 63 (2019), 103880, <https://doi.org/10.1016/j.nanoen.2019.103880>.

[28] W. Xu, Z. Lu, X. Sun, L. Jiang, X. Duan, Superwetting electrodes for gas-involving electrocatalysis, *Acc. Chem. Res.* 51 (2018) 1590–1598, <https://doi.org/10.1021/acs.accounts.8b00070>.

[29] M. Arif, G. Yasin, M. Shakeel, M.A. Mushtaq, W. Ye, X. Fang, S. Ji, D. Yan, Highly active sites of NiVB nanoparticles dispersed onto graphene nanosheets towards efficient and pH-universal overall water splitting, *J. Energy Chem.* 58 (2021) 237–246, <https://doi.org/10.1016/j.jecchem.2020.10.014>.

[30] G. Cai, W. Zhang, L. Jiao, S.-H. Yu, H.-L. Jiang, Template-directed growth of well-aligned MOF arrays and derived self-supporting electrodes for water splitting, *Chem* 2 (2017) 791–802, <https://doi.org/10.1016/j.chempr.2017.04.016>.

[31] D. Yu, L. Ge, B. Wu, L. Wu, H. Wang, T. Xu, Precisely tailoring ZIF-67 nanostructures from cobalt carbonate hydroxide nanowire arrays: toward high-performance battery-type electrodes, *J. Mater. Chem. A* 3 (2015) 16688–16694, <https://doi.org/10.1039/c5ta04509f>.

[32] D. Kim, X. Qin, B. Yan, Y. Piao, Sprout-shaped Mo-doped CoP with maximized hydrophilicity and gas bubble release for high-performance water splitting catalyst, *Chem. Eng. J.* 408 (2021), 127331, <https://doi.org/10.1016/j.cej.2020.127331>.

[33] B. Zhang, C. Li, J. Hu, D. Peng, K. Huang, J. Wu, Z. Chen, Y. Huang, Cobalt tungsten phosphide with tunable W-doping as highly efficient electrocatalysts for hydrogen evolution reaction, *Nano Res.* (2021), <https://doi.org/10.1007/s12274-021-3342-y>.

[34] T. Chen, S. Qin, M. Qian, H. Dai, Y. Fu, Y. Zhang, B. Ye, Q. Lin, Q. Yang, Defect-rich Fe-doped CoP nanosheets as efficient oxygen evolution electrocatalysts, *Energy Fuels* 35 (2021) 10890–10897, <https://doi.org/10.1021/acs.energyfuels.1c01301>.

[35] Q. Liang, K. Huang, X. Wu, X. Wang, W. Ma, S. Feng, Composition-controlled synthesis of Ni_{2-x}Co_xP nanocrystals as bifunctional catalysts for water splitting, *RSC Adv.* 7 (2017) 7906–7913, <https://doi.org/10.1039/c6ra26691f>.

[36] R. Zhang, X. Ren, S. Hao, R. Ge, Z. Liu, A.M. Asiri, L. Chen, Q. Zhang, X. Sun, Selective phosphidation: an effective strategy toward CoP/CeO₂ interface engineering for superior alkaline hydrogen evolution electrocatalysis, *J. Mater. Chem. A* 6 (2018) 1985–1990, <https://doi.org/10.1039/c7ta10237b>.

[37] L. Yan, B. Zhang, J. Zhu, Z. Liu, H. Zhang, Y. Li, Callistemon-like Zn and S codoped CoP nanorod clusters as highly efficient electrocatalysts for neutral-pH overall water splitting, *J. Mater. Chem. A* 7 (2019) 22453–22462, <https://doi.org/10.1039/c9ta08812a>.

[38] G. Zhou, X. Wu, M. Zhao, H. Pang, L. Xu, J. Yang, Y. Tang, Interfacial engineering-triggered bifunctionality of CoS₂/MoS₂ nanocubes/nanosheet arrays for high-efficiency overall water splitting, *ChemSusChem* 14 (2021) 699–708, <https://doi.org/10.1002/cssc.202002338>.

[39] S. Liu, H. Zhang, L. Xu, L. Ma, X. Hou, High lithium storage performance of Mn-doped Sn₄P₃ nanoparticles, *Electrochim. Acta* 210 (2016) 888–896, <https://doi.org/10.1016/j.electacta.2016.06.015>.

[40] P. Yadav, W. Malik, P.K. Dwivedi, L.A. Jones, M.V. Shelke, Electrosyn nanofibers of Tin Phosphide (SnP_{0.94}) nanoparticles encapsulated in a carbon matrix: a tunable conversion-cum-alloying lithium storage anode, *Energy Fuels* 34 (2020) 7648–7657, <https://doi.org/10.1021/acs.energyfuels.0c01046>.

[41] J. Li, S. Song, Y. Long, S. Yao, X. Ge, L. Wu, Y. Zhang, X. Wang, X. Yang, H. Zhang, A general one-pot strategy for the synthesis of Au@multi-oxide yolk@shell nanospheres with enhanced catalytic performance, *Chem. Sci.* 9 (2018) 7569–7574, <https://doi.org/10.1039/c8sc01520a>.

[42] M. Yang, C. Shang, F. Li, C. Liu, Z. Wang, S. Gu, D. Liu, L. Cao, J. Zhang, Z. Lu, H. Pan, Synergistic electronic and morphological modulation on ternary Co_{1-x}V_xP nanoneedle arrays for hydrogen evolution reaction with large current density, *Sci. China Mater.* 64 (2020) 880–891, <https://doi.org/10.1007/s40843-020-1495-x>.

[43] Y. Yan, J. Huang, X. Wang, T. Gao, Y. Zhang, T. Yao, B. Song, Ruthenium incorporated cobalt phosphide nanocubes derived from a prussian blue analog for enhanced hydrogen evolution, *Front. Chem.* 6 (2018) 521, <https://doi.org/10.3389/fchem.2018.00521>.

[44] D. Su, X. Zhang, A. Wu, H. Yan, Z. Liu, L. Wang, C. Tian, H. Fu, CoO-Mo₂N hollow heterostructure for high-efficiency electrocatalytic hydrogen evolution reaction, *NPG Asia Mater.* 11 (2019) 78, <https://doi.org/10.1038/s41427-019-0177-z>.

[45] S. Xie, F. Yang, H. Zhang, S. Wang, F. Cheng, X. Lu, Oxygen functionalized CoP nanowires as high-efficient and stable electrocatalyst for oxygen evolution reaction and full water splitting, *J. Electrochem. Soc.* 167 (2020), 124512, <https://doi.org/10.1149/1945-7111/abab24>.